PAPER

Anisotropic thermal conductivity in 2D tellurium

2D Materials

PAPER

RECEIVED
19 July 2019

REVISED
30 September 2019

ACCEPTED FOR PUBLICATION
17 October 2019

PUBLISHED
4 November 2019

Anisotropic thermal conductivity in 2D tellurium

Shouyuan Huang[1,2,7], Mauricio Segovia[1,2,7], Xiaolong Yang[1,3,7], Yee Rui Koh[2,4,5], Yixiu Wang[6], Peide D Ye[2,4], Wenzhuo Wu[2,6], Ali Shakouri[2,4], Xiulin Ruan[1,2,8] and Xianfan Xu[1,2,8]

[1] School of Mechanical Engineering, Purdue University, West Lafayette, IN 47907, United States of America
[2] Birck Nanotechnology Center, Purdue University, West Lafayette, IN 47907, United States of America
[3] Institute for Advanced Study, Shenzhen University, Shenzhen 518060, People's Republic of China
[4] School of Electrical and Computer Engineering, Purdue University, West Lafayette, IN 47907, United States of America
[5] Current address: Department of Mechanical and Aerospace Engineering, University of Virginia, Charlottesville, VI 22904, United States of America
[6] School of Industrial Engineering, Purdue University, West Lafayette, IN 47907, United States of America
[7] These authors contributed equally to this work.
[8] To whom correspondence should be addressed.

E-mail: ruan@purdue.edu **and** xxu@ecn.purdue.edu

Keywords: 2D-tellurium, thermal conductivity, thermoelectrics, micro-Raman thermometry

Supplementary material for this article is available online

Abstract

Two-dimensional tellurium (2D-Te) has been recently synthesized and shown potential in electronics, optoelectronics, and thermoelectric applications, with the merits of high mobility, environmental stability, high thermoelectric power-factor, and simplicity of mass production. These 2D-Te films have unique atomic structures: the Te atoms form trigonal helical chains and are then stacked into hexagonal lattice by van der Waals force, which brings up distinctive transport behaviors. Here we report anisotropic thermal conductivity of suspended 2D-Te films measured by micro-Raman thermometry and the time-domain thermal reflectance (TDTR) method. The in-plane along-chain and cross-chain thermal conductivities are found to be around 2.5 and 1.7 W m^{-1} K^{-1}, respectively, for thicker films (>100 nm), and reduced to 1.6 and 0.64 W m^{-1} K^{-1} for the thinner films (<20 nm). The measured anisotropy is >1.3 for all the films studied. The cross-plane (also across-chain) thermal conductivity is found to be around 0.8 to 1.2 W m^{-1} K^{-1} for thicker films, slightly lower than that along the in-plane across-chain direction due to the stronger suppression by the thin film boundary. Theoretical modeling reveals that the anisotropy mainly originates from anisotropic phonon dispersion. The long mean-free-path phonons in Te are also shown to be strongly suppressed by boundary scattering. The large reduction of anisotropic thermal conductivity from the bulk makes it the best single-element thermoelectric material and enables potential thermoelectric generation or cooling devices at room temperature. Our results also provide critical information for thermal management of 2D-Te electronic devices.

Introduction

The recently debuted two-dimensional tellurium (2D-Te) was found to be a high-mobility, environmentally stable material for novel transistors [1, 2]. As a sibling of graphene [3], transition-metal dichalcogenide [4], phosphorene [5, 6], etc, 2D-Te joined the intriguing family of 2D materials and has already shown engrossing bulk electronic properties of semiconducting [7, 8], photo-response [9], thermoelectricity [10, 11], and piezoelectricity [12]. Its application in transistors was first studied after the substrate-free solution process of large-area high-quality 2D-Te was developed [1]. A field-effect mobility value as high as 700 cm^2 V^{-1} s^{-1} at room temperature and a large ON-state current of 1 A mm^{-1} were observed on pristine flakes [1], and even higher performance CMOS devices were soon realized [13]. The high mobility enables near/mid-infrared photodetectors [14, 15]. Competitive piezoelectric [16] and thermoelectric [17] performances were also observed in 2D-Te devices that open the pathway to novel energy sources for wearable devices. It is also predicted that 2D-Te may exhibit multiple stable

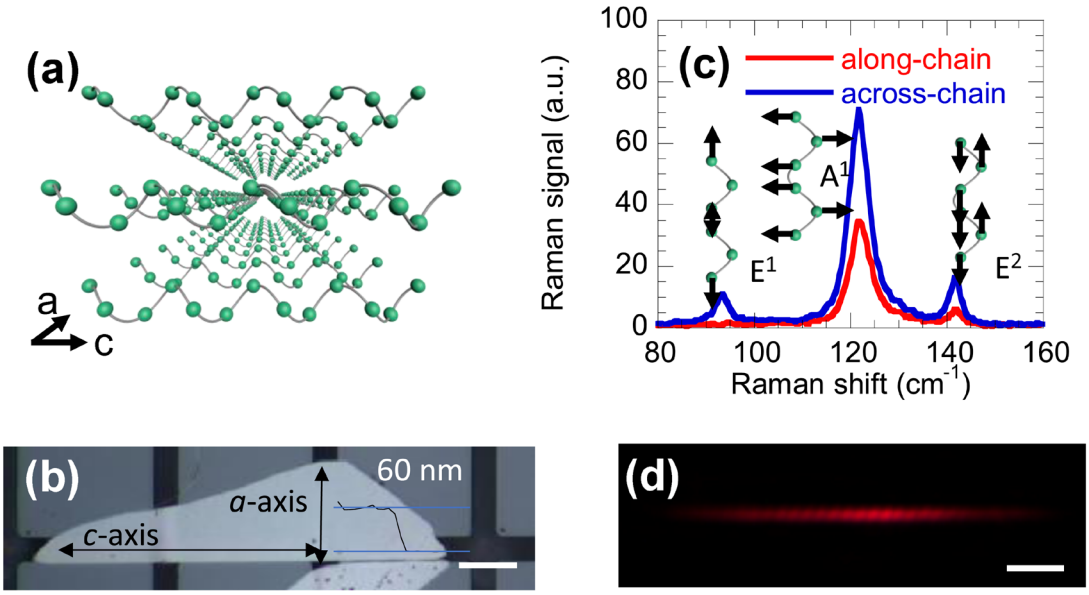

Figure 1. Characterization of tellurene thin films. (a) Illustration of the lattice structure of 2D-Te. (b) Optical microscope (AFM) image of 2D-Te (30 nm thick) transferred onto Si trench-grids. Scale bar: 10 μm. (c) Identification of lattice axes by polarized Raman spectra. (d) Optical image of the laser line. Scale bar: 5 μm.

phases that support diverse potential applications [18, 19].

The 2D-Te lattice is in the trigonal phase, the same as bulk Te. Each Te atom is covalently bonded to its two nearest neighbors in a trigonal helical chain, and individual chains are stacked together by the van der Waals (vdW) force (figure 1(a)). For atomic-thin Te layers, first-principle modeling also predicted 2D-Te has stable $\alpha/\beta/\gamma$-phases [18] with distinctive lattice structure that enables varied electrical and thermal properties, while experimental results of these transport properties have yet to be reported. In the 2D-Te we studied, the helical chains are in-plane, and the lattice configuration is like a 'bamboo raft'. The anisotropic transport properties naturally arise from the anisotropic atomic structures and bonding in the plane. Although the dynamics of this van der Waals (vdW) stacking helical chain lattice drew attention quite early [20, 21], its thermal conductivity of 2D-Te has never been reported, even rarely for the bulk. Thermal properties of annealed high-purity bulk tellurium were measured at the Thermophysical Properties Research Center, Purdue University in the 1970s, with room temperature thermal conductivity of 3.38 W m^{-1} K^{-1} in the *c*-axis (along-chain) and 1.97 W m^{-1} K^{-1} in the *a*-axis (across-chain) [22]. Thermal conductivity of polycrystalline tellurium was recently measured to be 1.6 W m^{-1} K^{-1} by the laser flash method [11]. First-principles calculations showed tellurium lattice thermal conductivity can be as low as 2.77 W m^{-1} K^{-1} (along-chain) and 1.22 W m^{-1} K^{-1} (across-chain) for (trigonal) bulk [23] and 4.08 W m^{-1} K^{-1} (zig-zag) and 2.16 W m^{-1} K^{-1} (armchair) for a single β-phase Te atomic layer [24], which has a stiffer bounding at room temperature.

Here we report the anisotropic thermal conductivity of the solution-grown 2D-Te. The in-plane anisotropy is inherited from the bulk lattice structure, i.e. the covalent bonds along-chain is stiffer and thus a higher thermal conductivity than the vdW interactions across-chain is expected. The cross-plane direction is also across-chain. Due to boundary scattering, the cross-plane thermal conductivity may also differ from the in-plane, cross-chain thermal conductivity. We employed the micro-Raman thermometry method [25], which was developed specifically to measure in-plane thermal conductivity of emerging 2D materials such as graphene [26, 27], transitional metal dichalcogenide [28, 29], hexagonal boron nitride [30], and few-layer black phosphorus [31]. The merit of this method is that it uses a much simpler sample preparation process than the methods involving micro-device fabrication [32, 33]. The optical phonon frequencies, due to bond softening and enhanced anharmonic phonon coupling, reduces when the temperature rises. This temperature-dependent Raman peak shift can be calibrated as a micro-optical thermometer. A laser is focused and illuminated at the center of the suspended thin-film, serving as both the heat source and a thermometer, and thermal conductivity can be then extracted using the Fourier law of heat conduction. The cross-plane thermal conductivity of thin films is measured using the time-domain thermal reflectance (TDTR) method [34–38]. The in-plane thermal conductivities are found to range from $\kappa_{//} \sim$ 1.6–2.5 W m^{-1} K^{-1} in the along-chain direction and $\kappa_{+} \sim$ 0.64–1.7 W m^{-1} K^{-1} in the across-chain direction, exhibiting anisotropy and thickness dependence. The cross-plane thermal conductivity is found to range from $\kappa_{\perp} \sim$ 0.8–1.2 W m^{-1} K^{-1}. First-principles calculations of thermal conductivity show that the observed anisotropy can be chiefly attributed to phonon dispersion while the over-all contribution of relaxation time of

phonon modes is almost independent on the lattice orientations. The longer (>10 nm) mean-free-path (MFP) acoustic phonons are strongly scattered by the surface, including possible surface phonon traps, leading to lower thermal conductivity in the cross-plane direction compared to that of the in-plane across-chain direction.

Results

Sample preparation and polarized Raman characterization

The 2D tellurium thin films studied in this work are grown through Na_2TeO_3 reduction by N_2H_4 in alkaline solution at elevated temperature [1, 39], then assembled into a single-layer continuous thin film through the Langmuir–Blodgett (LB) process [40]. The Te films are acquired on degreased glass slides, then transferred onto the dry-etched silicon trenches (figure 1(b)) using a capillary-assisted stamping method. The solution-grown tellurium films usually have a trapezoid shape, in which the parallel edges are along the chain. This can be verified by polarized Raman spectroscopy [1, 31]: a polarizer is placed at the entrance aperture of the spectrometer with its transmission axis along the incident laser polarization. The optical phonon modes are sensitive to the laser polarization due to the polarization selection rule arise from the lattice structure, and thus can be used to confirm the lattice orientation as shown in figure 1(c).

In-plane thermal transport measured using micro-Raman spectroscopy

We transfer solution-synthesized 2D-Te of 15–200 nm thickness and suspend them on 5 μm-wide silicon trench to measure the in-plane thermal conductivity of 2D-Te using the micro-Raman method. Using the polarized Raman spectroscopy described above, all the 2D-Te flakes studied have <5° of its chain axis aligned to the trenches. Atomic force microscope mapping is conducted on multiple edges to obtain thickness and verify uniformity.

The temperature dependence of the peak shift of the A1 Raman mode is used as a microscale optical thermometer. The sample is first installed in a heating stage to calibrate the Raman peak shift (ω) versus temperature (θ), excited with a 633 nm laser ~15 μW to minimize the temperature rise. Both along-chain and across-chain directions are calibrated, and it is found that the A1 mode with cross-chain laser polarization offers the largest Raman peak shift versus temperature change (figure 2(a)), and is thus chosen for the subsequent temperature measurements. With small temperature rises use in the experiments, the temperature dependent Raman frequency can be expressed in a linear form $\omega = \omega_0 + \chi\theta$. We notice that Raman shift is also sensitive to strain. As a result, the temperature coefficient χ is specific to the mechanical condition in which the calibration is performed (i.e. suspended, stress-free due to thin shell buckling), and calibration and actual thermal transport measured are performed in the exact same condition [41].

All micro-Raman in-plane thermal conductivity measurements are performed at room temperature. A 50 μm-wide slit is placed in the laser beam path to create a line-shape laser beam at the focal point (figure 1(d)). The laser intensity distributions are Gaussian along both directions, and the widths are characterized to be 0.98 and 9.6 μm, respectively (supplemental note 1 (stacks.iop.org/TDM/7/015008/mmedia)). The line-shaped laser beam is aligned to the center of the trench, creating a quasi-1D heat flow perpendicular to the trench in the suspended 2D-Te film. In this scenario, heat flow in the 2D-Te film is dominated by the conduction in one lattice orientation, isolating the anisotropic thermal conductivity.

We collect a series of Raman spectra, which is then converted to the temperature rise using the calibrated χ, with increasing incident laser power. A typical Raman shift versus incident laser power for a 35 nm thick film is shown in figure 2(b). The absorbed laser power is also needed for thermal conductivity extraction, and is measured for each individual film by measuring reflection, R and transmission, T. The details and the results are provided in supplementary note 2. We then obtain the relation between temperature rise versus absorbed power which is used to extract the thermal conductivity as described below.

The 3D heat conduction model, equation (1), is used to extract in-plane thermal conductivity, even though heat flow is dominant along one direction by using a line-shape laser beam. The Gaussian laser heat source is given by equation (2), where A is the absorbance, w_0 and l_0 represent the width and length of the laser focal line, and w and l are the coordinates.

$$\frac{\partial}{\partial x}\left(k_x\frac{\partial\theta}{\partial x}\right)+\frac{\partial}{\partial y}\left(k_y\frac{\partial\theta}{\partial y}\right)+\frac{\partial}{\partial z}\left(k_z\frac{\partial\theta}{\partial z}\right)+\dot{q}=0 \tag{1}$$

$$\dot{q}''=\frac{AP_i}{\pi w_0 l_0 t}e^{-\left(\frac{2w^2}{w_0^2}+\frac{2l^2}{l_0^2}\right)} \tag{2}$$

$$\theta_{Raman}=\frac{\int_0^\infty\int_0^\infty \theta e^{-\left(\frac{2w^2}{w_0^2}+\frac{2l^2}{l_0^2}\right)}\,\mathrm{d}w\mathrm{d}l}{\int_0^\infty\int_0^\infty e^{-\left(\frac{2w^2}{w_0^2}+\frac{2l^2}{l_0^2}\right)}\,\mathrm{d}w\mathrm{d}l}. \tag{3}$$

The measured temperature rise is a Gaussian-weighted average temperature per the laser focal line intensity distribution, per equation (3). In equations (2) and (3), the laser heating and the temperature in the z-direction are assumed to be uniform, due to the thickness being small comparing to the other two directions. The experimentally measured temperature rise versus absorbed power, $\mathrm{d}\theta_{\mathrm{Raman}}/\mathrm{d}P_A$, is compared with the calculated slope to find the thermal conductivities. $\kappa_{//}$ and κ_{+} are extracted by an iterative procedure (supplementary note 1, figure S2) because the thermal conductivity along the trench also weakly affects the temperature rise due to the finite length of the line

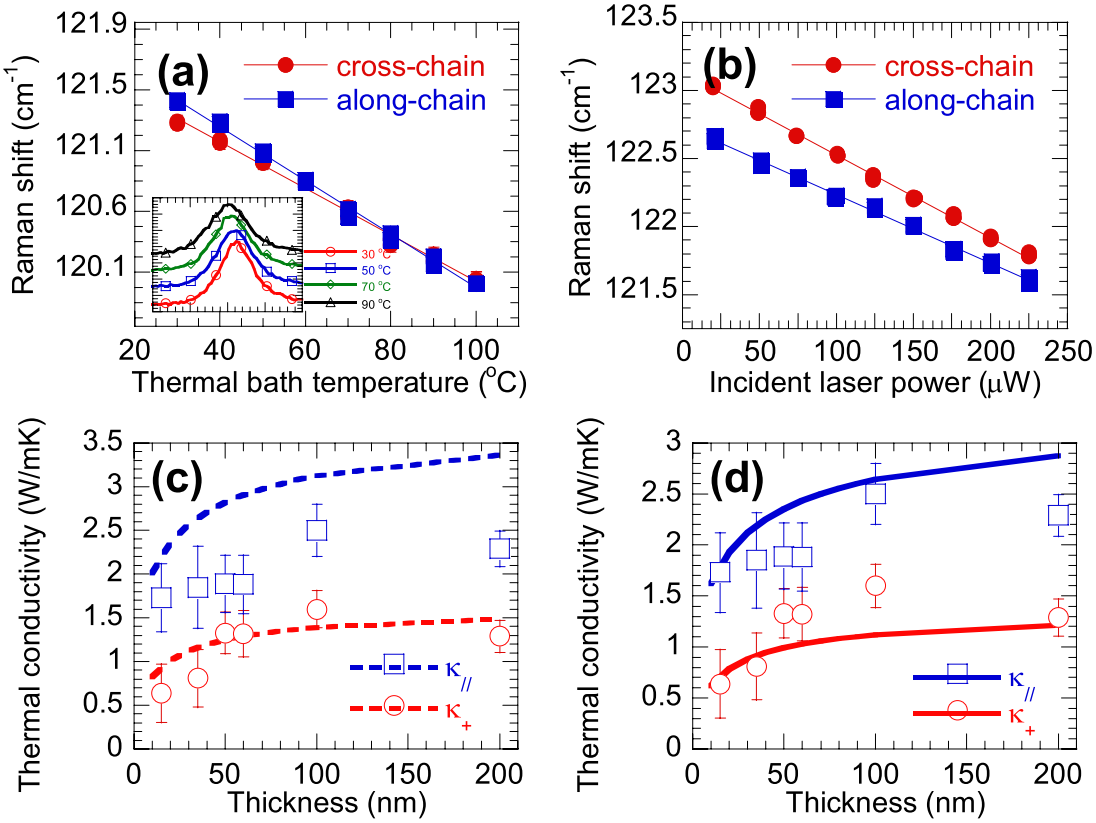

Figure 2. Measurement of 2D-Te in-plane thermal conductivity using micro-Raman thermometry method. (a) Raman shift of A1 mode as a function of temperature with laser polarization along the chain and across the chain. The lines represent linear fitting. Inset: four sample Raman spectra taken at varies bath temperatures. (b) Raman shift of A1 mode, representing Raman temperature rise, as a function of incident laser power. The lines represent the linear fitting. (c) Extracted in-plane thermal conductivities ($\kappa_{//}, \kappa_{+}$) of multiple 2D-Te films. Dashed lines are from first-principle calculations assuming no defects. (d) Extracted in-plane anisotropic thermal conductivity compared with first-principle prediction assuming a 0.1% defect level.

laser. The extracted in-plane thermal conductivities are presented in figures 2(c) and (d), which show an apparent thickness-dependence and anisotropy. The relative uncertainty of in-plane thermal conductivity is ~20% for the thinnest film and reduced to <5% for thicker flakes. The details of the uncertainty analysis are given in supplementary note 3. Results from the first-principles predictions assuming diffuse boundary scattering are also shown in figures 2(c) and (d) as a comparison, and will be discussed later.

Cross-plane thermal transport measured using TDTR method

To measure the cross-plane thermal conductivity, tellurium flakes of varied thicknesses from the same batch for the in-plane thermal conductivity measurements are used. 2D-Te films with thicknesses about 50–200 nm are transferred to an ultra-clean silicon wafer and then coated with 70 nm of aluminum by electron-beam evaporation. Not enough sensitivity can be obtained for the films less than 50 nm (supplementary note 3). The cross-plane thermal conductivity is measured using the femtosecond time-domain thermoreflectance (TDTR) technique [34–36, 42] (see Method for details). Figure 3(a) presents a typical (a 165 nm 2D-Te film) TDTR measurement data, the ratio of in-phase/out-of-phase signal versus the delay time, fitted by the heat transfer model. The measured cross-plane thermal conductivities of films with various thicknesses are shown in figure 3(b), together with the first-principle calculations which will be discussed below. The uncertainty of the fitting is about ±0.1 W $m^{-1} K^{-1}$ for thicker films and is about ±0.3 W $m^{-1} K^{-1}$ for thinner films. The uncertainty propagation analysis is given in supplementary note 3.

Discussion

The anisotropic thermal conductivity are summarized in figures 2(c) and 3(b). We attribute the thermal conductivity largely to the lattice contribution, because the electronic thermal conductivity is estimated to be ~0.1 W $m^{-1} K^{-1}$ using electrical conductivity [17] and Wiedemann–Franz Law assuming the Lorenz number between the single-band/nondegenerate and metal/highly-degenerated limits. The thermal conductivity along the chain of the stiff covalent bond $\kappa_{//}$ is 50%–150% higher than that in the vdW bonded across-chain direction κ_{+} and $\kappa_{\perp}$. The anisotropic phonon dispersion in the along-chain (Γ–*A* or [0 0 0 1]) direction and the across-chain direction originates from the contrasting bonding condition, and is the main reason of this anisotropy of

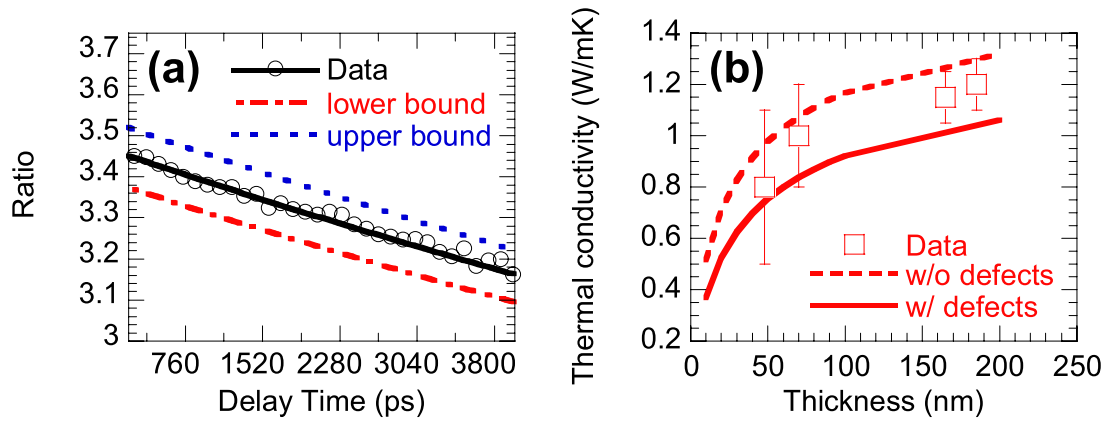

Figure 3. Measurement of cross-plane thermal conductivity using TDTR method. (a) Typical thermal reflectance trace in the time domain, curve fitted with best-fit thermal conductivity and its upper and low bounds. (b) Extracted cross-plane thermal conductivity of 2D-Te films at varies thicknesses, with first-principle predictions with (0.1% defects) and without defects.

thermal conductivity. In addition, phonon transport in the cross-chain direction (both in-plane and out-of-plane) is suppressed more from surface scattering, as discussed further below. $\kappa_{//}$ is ~2.5 W m^{-1} K^{-1} for the near-bulk 100 nm thick film and reduces to ~1.6 W m^{-1} K^{-1} as film thickness decreases to 15 nm. Similar thickness dependence also observed κ_{+} and $\kappa_{\perp}$, decreasing from ~1.7 and 1.2 W m^{-1} K^{-1} to 0.6 and 0.8 W m^{-1} K^{-1}, respectively. This size-effect indicates strong surface scattering of long-MFP phonons. The surface scattering also affects electronic transport that reduced mobility, which is observed for thinner 2D-Te films [1]. In a similar material Bi_2Te_3 thin films, strong size effects of electronic and thermal transport due to surface scattering were also observed [43]. Compared with the experimental result of bulk thermal conductivity of $\kappa_{//} = 3.38$ W m^{-1} K^{-1}, $\kappa_{+} = 1.97$ W m^{-1} K^{-1} [22] and first-principle calculated values of $\kappa_{//} = 2.77$ W m^{-1} K^{-1}, $\kappa_{+} = 1.22$ W m^{-1} K^{-1} at room temperature [23], the values of the measured thermal conductivity of all samples are lower.

First-principle calculations are carried out to help to understand the measured thermal transport properties. Figure 4(a) shows the calculated optimized structure of trigonal tellurium, which has a monoclinic phase with space group P_{3121}, and consists of helical chains arranged in a hexagonal array along the *c*-axis as seen earlier in figure 1(a), while the *a*-axis is in the in-plane, cross chain direction and the *b*-axis in the cross-plane (both perpendicular to the helical chains). Specifically, the intrachain and interchain distances are found to be 2.89 and 3.50 Å. The phonon dispersion and group velocities are shown in figures 4(b) and (c), respectively. As is seen in figure 4(c), group velocities along the chain direction are much larger than the other two directions, especially for phonons with frequency below 2 THz. The relaxation time of the modes contributing to the $\kappa_{//}$ and κ_{+} are presented in figure 4(d), demonstrating a small difference along different directions. Thus, we conclude that the thermal conductivity anisotropy in the bulk is chiefly attributed to the anisotropic group velocity. We also show the calculated cumulative thermal conductivity of bulk Te at room temperature in figure 4(e), with the bulk values of $\kappa_{//}$ and κ_{+} approaching 3.72 and 1.63 W m^{-1} K^{-1}, respectively, which agree better with the measurement result of bulk ($\kappa_{//} = 3.38$ W m^{-1} K^{-1}, $\kappa_{+} = 1.97$ W m^{-1} K^{-1}) [22] than previous prediction [23]. Notice that (figure 4(e)) the contribution from long-MFP-phonons greater than 1 μm is inevitably reduced by defects, thus, the cumulative phonon $\kappa_{//}$ at 1.5 μm, 3.36 W m^{-1} K^{-1} agrees well with the measurement of bulk. The difference in the bulk thermal conductivity between our prediction and previous calculation is mainly attributed to the differences in pseudopotentials and parameter settings. Compared to literature [23], our prediction used projector augmented wave (PAW) potential under the generalized gradient approximation (GGA) for exchange-correlation functional to compute the second and third-order interatomic force constants (IFCs), and phonon scattering rates were calculated in a denser reciprocal space with a 24 × 24 × 24 q-mesh, which agree better with the experimental values [22] considering the electron thermal conductivity of about 0.1 W m^{-1} K^{-1}. It can also be seen that thermal conductivities of Te are mainly dominated by phonons with MFP below 100 nm (corresponds to 2 THz). This is the reason that the thermal conductivities of Te film are greatly affected by boundary scattering when the film thickness is below 100 nm.

The anisotropic thermal conductivities of 2D-Te films at room temperature are calculated considering the mode-wise effects from diffuse surface scattering (figures 2(c) and 3(b)). The measured data overall follows the trend of the predicted classical size effect, while the generally lower values from experiments are attributed to defects. Figure 4(f) shows the relative thermal conductivity as a function of the thickness of 2D-Te films. It can be observed that the cross-plane κ is reduced more than the other two directions due to additional scattering at the surface. For in-plane transport, $\kappa_{//}$ and κ_{+} are reduced to 80% of the bulk value for

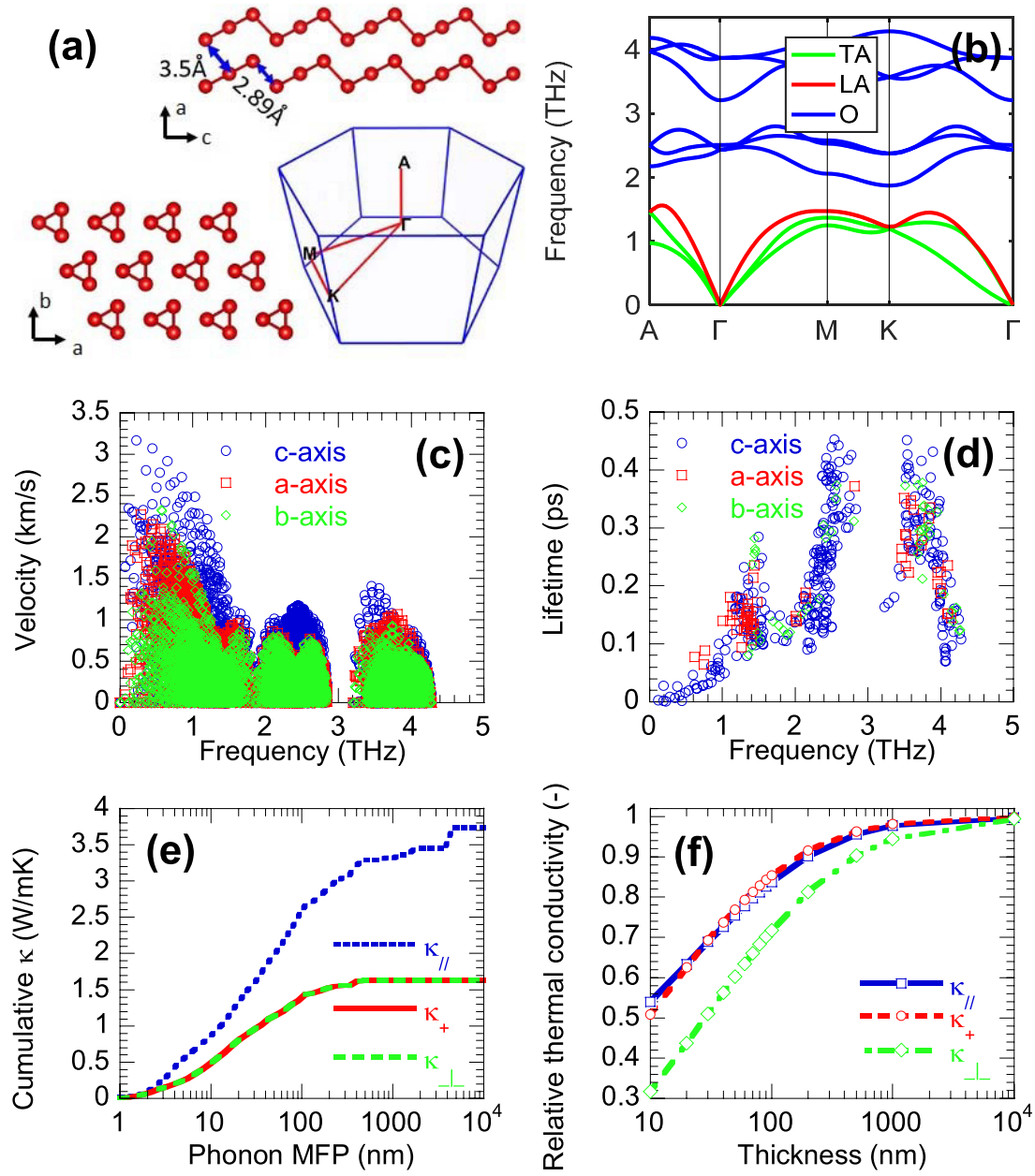

Figure 4. Modeling results of 2D-Te based on first-principle calculation. (a) Lattice structure and first-Brillion zone of trigonal tellurium. (b) Phonon dispersion of bulk trigonal tellurium on high-symmetry axes. (c) Phonon group velocities of the three directions as a function of frequency ω. (d) Relaxation time of phonon modes along different directions. (e) Cumulative thermal conductivity of bulk Te as a function of phonon MFP. (f) Relative thermal conductivities with increasing thickness of Te film.

100 nm-thick film, while the cross-plane $\kappa_{\perp}$ is reduced to 70%. As the thickness decreases to 10 nm, we find that the $\kappa_{//}$, κ_{+}, and $\kappa_{\perp}$ values sharply decrease to about 53%, 50% and 32%, respectively. In the cross-plane direction, although it is also cross-chain, the thermal conductivity is reduced more than that of the in-plane cross-chain direction. This is because the boundary is perpendicular to the cross-plane $\kappa_{\perp}$ direction, hence shortens the mean free path of the corresponding phonons more. In [44], a similar scenario of dielectric thin film was observed. The effects of boundary scattering for reducing the thermal transport in different directions can be further characterized using the suppression function [44–46] (supplementary note 4).

The measured data in the three directions are generally lower than the calculation values and show some fluctuations with the thickness as mentioned above. We attribute these to the defects in 2D-Te films which is may not be homogeneous for different samples. Comparing with the first-principle calculation that accounts for the point defects, we found that the reduction of thermal conductivity can be roughly fit at a defect level of about 0.1% (figure 2(d)), which is reasonable for liquid-phase synthesized thin films [47]. We also notice that recent proposals of covalent-like quasi-bonding, an inter-chain interaction with wavefunction hybridization stronger than the vdW force [19, 48], which rises especially when Te or Se approaching

2D thin-film, may explain the smaller difference of $\kappa_{//}$ and κ_{+} than first-principle prediction.

To conclude, we measured the anisotropic thermal conductivities of 2D-Te in the in-plane along/across chain directions, as well as the cross-plane direction using micro-Raman thermometry and TDTR, and studied the phonon transport processes using the first-principle-based simulation. The thermal conductivities are intrinsically anisotropic and reduced by as much as 60% as the thickness decreases from 200 nm to 15 nm due to surface scattering of phonons, especially long-MFP phonons, while the anisotropy arises in the both in-plane and cross-plane directions. Theoretical modeling of phonon dynamics illustrated that the anisotropy is chiefly attributed to the anisotropy phonon dispersion which stems from the contrast of covalent bond versus vdW interaction. The results reported here indicates the prospective of 2D-Te based high-performance thermoelectric generator/cooler at room temperature, also will support essential parameters for designing thermal systems for 2D-Te transistors and other electronic devices.

Methods

Sample preparation

2D-Te is synthesized using a substrate-free solution process, then scooped onto 285 nm SiO_2/Si substrate from the Langmuir–Blodgett (LB) assembled water-air interface. Details can be found in [1]. The 2D-Te films are then transferred using capillary-force-assisted PDMS method after rinsing with toluene, acetone, and isopropanol. 2 mm PDMS is cured on degreased glass slides and held above heated water to collect the water vapor, then place gently on the SiO_2/Si substrate. The films can be peeled off with the PDMS maintaining a small angle, and then be transferred onto the Si trench-grid by stamping under the optical microscope. Details of the transfer method can be found in [49]. The aforementioned Si trench-grid is fabricated by SF_6/C_4F_8 deep reactive ion etching (STS Advanced Silicon Etcher) of a silicon wafer patterned by photolithography (2 μm AZ-1518 photoresist, developed by MF-26A). AFM and SEM images were taken by an AIST-NT Combi Scope system and an FEI Nova system respectively.

Raman measurements

The micro-Raman thermometry was conducted using a Horiba LabRam HR800 spectrometer system coupled to an Olympus microscope with a 100× objective. A 632.8 nm He-He laser was used to excite Raman scattering, also as the heating source. An 1800 1/mm grating was used to give a ~0.27 cm^{-1} per nominal spectral resolution. The polarized Raman measurement was done with a linear polarizer (Thorlabs, LPNIRE050-B) placed at the entrance aperture of the spectrometer as the analyzer. The Lorentzian fitting of the Raman spectra give the Raman peak positions with uncertainties $<0.015\,cm^{-1}$, i.e. temperature resolution <1 K per the Raman-temperature calibration. The absorption was measured on 2D-Te films from the same batch suspended on degreased cover glass slides. The reflectivity was measured by the same laser using a silver-coated mirror as a reference with known reflectivity, while the transmissivity of the sample was obtained by a photo-power meter placed underneath it. The optical properties of 2D-Te were derived using the optical multilayer film theory. Then absorbed laser power was calculated from the optical properties and the total incident laser power, and subsequently used as the heat source input for the numerical heat transfer model to extract the in-plane thermal conductivity of the suspended thin film. The optical properties measurement details are reported in supplementary note 2. This method is adapted from our previous works [25, 31, 41].

Thermal reflectance measurements

The TDTR measurement was conducted using a Ti: Sapphire femtosecond laser wavelength centered at 800 nm with a 100 fs duration pulse laser at a repetition rate of ~80 MHz. The train of laser pulses is split into a pump beam and a probe beam using a beam splitter. Each beam is then linearly polarized with different orientations. The pump beam is then modulated at a frequency of 824 kHz, and passed through a delay stage creating a controlled delay between pump and probe pulses. The modulated pump beam and non-modulated probe beam are then brought in focus to the surface of the coated sample. The radii of the focused pump and probe laser beams are ~6 μm and ~5.5 μm respectively. A ~70 nm thick aluminum film is deposited on the 2D-Te as an optical absorption layer and thermal reflectance transducer. The reflected light is filtered through a polarizer to allow only the probe light through, and the probe light is detected by a Si-photodetector. An RF lock-in amplifier is used to lock into the frequency of the modulated pump. Both the in-phase and out-of-phase signals (indicating the temporal change at the Al surface) are used to extract the cross-plane thermal conductivity by fitting to a 2D transient heat diffusion model. A 2D transient heat diffusion equation is used to fit the temporal temperature change at the surface to extract the thermal conductivity of the sample.

First-principle based theoretical calculation

The details of theoretical calculation are given in supplementary note 4.

Acknowledgments

X Xu and P D Ye acknowledge the support from the AFOSR/NSF 2DARE program. S Huang and X Xu are also supported in part by the NSF 1462622-CMMI project. P D Ye is also supported in part by US

Army Research Office and in part by ASCENT, one of six centers in JUMP, a Semiconductor Research Corporation (SRC) program sponsored by DARPA. X L Ruan acknowledges the partial support from The Defense Advanced Research Projects Agency (Award No. HR0011-15-2-0037). X L Yang acknowledges the support from the China Scholarship Council. The synthesis of 2D Te materials is supported by the National Science Foundation under Grant CMMI-1762698.

Competing financial interests statement

The authors declare no competing financial interests.

ORCID iDs

Xianfan Xu https://orcid.org/0000-0003-0580-4625

References

[1] Wang Y *et al* 2018 Field-effect transistors made from solution-grown two-dimensional tellurene *Nat. Electron.* **1** 228–36
[2] Du Y, Qiu G, Wang Y, Si M, Xu X, Wu W and Ye P D 2017 One-dimensional van der Waals material tellurium: Raman spectroscopy under strain and magneto-transport *Nano Lett.* **17** 3965–73
[3] Novoselov K S, Geim A K, Morozov S V, Jiang D, Zhang Y, Dubonos S V, Grigorieva I V and Firsov A A 2004 Electric field effect in atomically thin carbon films *Science* **306** 666–9
[4] Mak K F, Lee C, Hone J, Shan J and Heinz T F 2010 Atomically thin MoS_2 : a new direct-gap semiconductor *Phys. Rev. Lett.* **105** 136805
[5] Liu H, Neal A T, Zhu Z, Luo Z, Xu X, Tomanek D and Ye P D 2014 Phosphorene: an unexplored 2D semiconductor with a high hole mobility *ACS Nano* **8** 4033–41
[6] Li L, Yu Y, Ye G J, Ge Q, Ou X, Wu H, Feng D, Chen X H and Zhang Y 2014 Black phosphorus field-effect transistors *Nat. Nanotechnol.* **9** 372–7
[7] Bottom V E 1952 The Hall effect and electrical resistivity of tellurium *Science* **115** 570–1
[8] Von Klitzing K and Landwehr G 1971 Magnetic freeze-out and magnetoresistance of tellurium in strong magnetic fields *Phys. Status Solidi* **45** K119–22
[9] Liu J-W, Zhu J-H, Zhang C-L, Liang H-W and Yu S-H 2010 Mesostructured assemblies of ultrathin superlong tellurium nanowires and their photoconductivity *J. Am. Chem. Soc.* **132** 8945–52
[10] Peng H, Kioussis N and Snyder G J 2014 Elemental tellurium as a chiral p-type thermoelectric material *Phys. Rev.* B **89** 195206
[11] Lin S, Li W, Chen Z, Shen J, Ge B and Pei Y 2016 Tellurium as a high-performance elemental thermoelectric *Nat. Commun.* **7** 10287
[12] Royer D and Dieulesaint E 1979 Elastic and piezoelectric constants of trigonal selenium and tellurium crystals *J. Appl. Phys.* **50** 4042–5
[13] Qiu G, Si M, Wang Y, Lyu X, Wu W and Ye P D 2018 High-performance few-layer tellurium CMOS devices enabled by atomic layer deposited dielectric doping technique *2018 76th Device Res. Conf.*
[14] Amani M *et al* 2018 Solution-synthesized high-mobility tellurium nanoflakes for short-wave infrared photodetectors *ACS Nano* **12** 7253–63
[15] Deckoff-Jones S, Wang Y, Lin H, Wu W and Hu J 2019 Tellurene: a multifunctional material for midinfrared optoelectronics *ACS Photonics* **6** 1632–8
[16] Gao S, Wang Y, Wang R and Wu W 2017 Piezotronic effect in 1D van der Waals solid of elemental tellurium nanobelt for smart adaptive electronics *Semicond. Sci. Technol.* **32** 104004
[17] Qiu G, Huang S, Segovia M, Venuthurumilli P K, Wang Y, Wu W, Xu X and Ye P D 2019 Thermoelectric performance of 2D tellurium with accumulation contacts *Nano Lett.* **19** 1955–62
[18] Zhu Z *et al* 2017 Multivalency-driven formation of Te-based monolayer materials: a combined first-principles and experimental study *Phys. Rev. Lett.* **119** 106101
[19] Xiang Y, Gao S, Xu R-G, Wu W and Leng Y 2019 Phase transition in two-dimensional tellurene under mechanical strain modulation *Nano Energy* **58** 202–10
[20] Pine A S and Dresselhaus G 1971 Raman spectra and lattice dynamics of tellurium *Phys. Rev.* B **4** 356–71
[21] Martin R M, Lucovsky G and Helliwell K 1976 Intermolecular bonding and lattice dynamics of Se and Te *Phys. Rev.* B **13** 1383–95
[22] Ho C Y, Powell R W and Liley P E 1972 Thermal conductivity of the elements *J. Phys. Chem. Ref. Data* **1** 279–421
[23] Peng H, Kioussis N and Stewart D A 2015 Anisotropic lattice thermal conductivity in chiral tellurium from first principles *Appl. Phys. Lett.* **107** 251904
[24] Gao Z, Tao F and Ren J 2018 Unusually low thermal conductivity of atomically thin 2D tellurium *Nanoscale* **10** 12997–3003
[25] Luo Z, Liu H, Spann B T, Feng Y, Ye P, Chen Y P and Xu X 2014 Measurement of in-plane thermal conductivity of ultrathin films using micro-Raman spectroscopy *Nanoscale Microscale Thermophys. Eng.* **18** 183–93
[26] Balandin A A, Ghosh S, Bao W, Calizo I, Teweldebrhan D, Miao F and Lau C N 2008 Superior thermal conductivity of single-layer graphene: geim *Nano Lett.* **8** 902–7
[27] Cai W, Moore A L, Zhu Y, Li X, Chen S, Shi L and Ruoff R S 2010 Thermal transport in suspended and supported monolayer graphene grown by chemical vapor deposition *Nano Lett.* **10** 1645–51
[28] Yan R, Simpson J R, Bertolazzi S, Brivio J, Watson M, Wu X, Kis A, Luo T, Walker A R H and Xing H G 2014 Thermal conductivity of monolayer molybdenum disulfide obtained from temperature-dependent Raman spectroscopy *ACS Nano* **8** 986–93
[29] Sahoo S, Gaur A P S, Ahmadi M, Guinel M J F and Katiyar R S 2013 Temperature-dependent Raman studies and thermal conductivity of few-layer MoS_2 *J. Phys. Chem.* C **117** 9042–7
[30] Zhou H *et al* 2014 High thermal conductivity of suspended few-layer hexagonal boron nitride sheets *Nano Res.* **7** 1232–40
[31] Luo Z, Maassen J, Deng Y, Du Y, Garrelts R P, Lundstrom M S, Ye P D and Xu X 2015 Anisotropic in-plane thermal conductivity observed in few-layer black phosphorus *Nat. Commun.* **6** 8572
[32] Shi L, Li D, Yu C, Jang W, Kim D, Yao Z, Kim P and Majumdar A 2003 Measuring thermal and thermoelectric properties of one-dimensional nanostructures using a microfabricated device *J. Heat Transfer* **125** 881
[33] Kim P, Shi L, Majumdar A and McEuen P L 2001 Thermal transport measurements of individual multiwalled nanotubes *Phys. Rev. Lett.* **87** 215502
[34] Cahill D G 2004 Analysis of heat flow in layered structures for time-domain thermoreflectance *Rev. Sci. Instrum.* **75** 5119–22
[35] Kang K, Koh Y K, Chiritescu C, Zheng X and Cahill D G 2008 Two-tint pump-probe measurements using a femtosecond laser oscillator and sharp-edged optical filters *Rev. Sci. Instrum.* **79** 114901
[36] Schmidt A J, Chen X and Chen G 2008 Pulse accumulation, radial heat conduction, and anisotropic thermal conductivity in pump-probe transient thermoreflectance *Rev. Sci. Instrum.* **79** 1–9
[37] Zhu J, Tang D, Wang W, Liu J, Holub K W and Yang R 2010 Ultrafast thermoreflectance techniques for measuring thermal conductivity and interface thermal conductance of thin films *J. Appl. Phys.* **108** 094315
[38] Garrelts R, Marconnet A and Xu X 2015 Assessment of thermal properties via nanosecond thermoreflectance method *Nanoscale Microscale Thermophys. Eng.* **19** 245–57
[39] Wang Y, de Souza Borges Ferreira R, Wang R, Qiu G, Li G, Qin Y, Ye P D, Sabbaghi A and Wu W 2019 Data-driven and probabilistic learning of the process-structure-property

relationship in solution-grown tellurene for optimized nanomanufacturing of high-performance nanoelectronics *Nano Energy* **57** 480–91
[40] Zasadzinski J A, Viswanathan R, Madsen L, Garnaes J and Schwartz D K 1994 Langmuir–Blodgett films *Science* **263** 1726
[41] Luo Z, Tian J, Huang S, Srinivasan M, Maassen J, Chen Y P and Xu X 2018 Large enhancement of thermal conductivity and Lorenz number in topological insulator thin films *ACS Nano* **12** 1120–7
[42] Zhao D, Qian X, Gu X, Jajja S A and Yang R 2016 Measurement techniques for thermal conductivity and interfacial thermal conductance of bulk and thin film materials *J. Electron. Packag.* **138** 040802
[43] Pettes M T, Maassen J, Jo I, Lundstrom M S and Shi L 2013 Effects of surface band bending and scattering on thermoelectric transport in suspended bismuth telluride nanoplates *Nano Lett.* **13** 5316–22
[44] Majumdar A 1993 Microscale heat conduction in dielectric thin films *J. Heat Transfer* **115** 7
[45] Carrete J, Vermeersch B, Katre A, van Roekeghem A, Wang T, Madsen G K H and Mingo N 2017 almaBTE : a solver of the space–time dependent Boltzmann transport equation for phonons in structured materials *Comput. Phys. Commun.* **220** 351–62
[46] Dongre B, Carrete J, Mingo N and Madsen G K H 2018 *Ab initio* lattice thermal conductivity of bulk and thin-film α-Al_2O_3 *MRS Commun.* **8** 1119–23
[47] Lin Z *et al* 2016 2D materials advances: from large scale synthesis and controlled heterostructures to improved characterization techniques, defects and applications *2D Mater.* **3** 042001
[48] Qiao J, Pan Y, Yang F, Wang C, Chai Y and Ji W 2018 Few-layer tellurium: one-dimensional-like layered elementary semiconductor with striking physical properties *Sci. Bull.* **63** 159–68
[49] Ma X, Liu Q, Xu D, Zhu Y, Kim S, Cui Y, Zhong L and Liu M 2017 Capillary-force-assisted clean-stamp transfer of two-dimensional materials *Nano Lett.* **17** 6961–7